MIT Libraries | DSpace@MIT

MIT Open Access Articles

Near-Ambient Pressure XPS of High-Temperature Surface Chemistry in Sr2Co2O5 Thin Films

Massachusetts Institute of Technology

Near-ambient pressure XPS of high-temperature surface chemistry in $Sr_2Co_2O_5$ thin films

Wesley T. Hong* · Kelsey A. Stoerzinger* · Ethan J. Crumlin · Eva Mutoro · Hyoungjeen Jeen · Ho Nyung Lee · Yang Shao-Horn

Abstract

Transition metal perovskite oxides are promising electrocatalysts for the oxygen reduction reaction (ORR) in fuel cells, but a lack of fundamental understanding of oxide surfaces impedes the rational design of novel catalysts with improved device efficiencies. In particular, understanding the surface chemistry of oxides is essential for controlling both catalytic activity and long-term stability. Thus, elucidating the physical nature of A-site enriched species on perovskite surfaces and their catalytic enhancement would generate new insights in developing oxide electrocatalysts. In this article, we perform near-ambient pressure XPS of model brownmillerite $Sr_2Co_2O_5$ (SCO) epitaxial thin films with different crystallographic orientations. Detailed analysis of the Co $2p$ spectra suggests that the films lose oxygen as a function of temperature. Moreover, deconvolution of the O $1s$ spectra shows distinct behavior for (114)-oriented SCO films compared to (001)-oriented SCO films, where an additional bulk oxygen species is observed. These findings indicate a change to a perovskite-like oxygen chemistry that occurs more easily in (114) SCO than (001) SCO, likely due to the orientation of oxygen vacancy channels out-of-plane with respect to the film surface. This difference in surface chemistry is responsible for the anisotropy of the oxygen surface exchange coefficient of SCO and may contribute to the enhanced ORR kinetics of $La_{0.8}Sr_{0.2}CoO_{3-\delta}$ thin films by SCO surface particles observed previously.

Keywords

ambient pressure XPS · strontium cobaltite · solid oxide fuel cells · oxygen reduction · electrocatalysis

Wesley T. Hong · Kelsey A. Stoerzinger
Department of Materials Science & Engineering, Massachusetts Institute of Technology, Cambridge, MA, USA

Ethan J. Crumlin
Advanced Light Source, Lawrence Berkeley National Laboratory, Berkeley, CA, USA

Eva Mutoro
BASF SE, Ludwigshafen, Germany

Hyoungjeen Jeen

Materials Science and Technology Division, Oak Ridge National Laboratory, Oak Ridge, TN, USA and Department of Physics, Pusan National University, Busan, Korea

Ho Nyung Lee
Materials Science and Technology Division, Oak Ridge National Laboratory, Oak Ridge, TN, USA

Yang Shao-Horn
Department of Mechanical Engineering, Department of Materials Science & Engineering, Massachusetts Institute of Technology, Cambridge, MA, USA
e-mail: shaohorn@mit.edu

*These authors contributed equally to this manuscript.

1 Introduction

Transition metal perovskite oxides are studied extensively as electrocatalysts for the oxygen reduction reaction (ORR) in fuel cells, which may enable the development of cost-effective and clean conversion technologies [1, 2]. However, a lack of fundamental understanding of the electrocatalytic mechanism on oxide surfaces has impeded the rational design of novel, highly active catalysts to improve device efficiencies. A large body of work has come out of the solid oxide fuel cell community on the surface chemistry of perovskite oxides aiming to understand how tuning the perovskite surface can modify the kinetics of oxygen reduction ($O_2 + 4e^- \rightarrow 2O^{2-}$) at high temperatures [3, 4]. Many studies suggest that the influence of A-site cation enrichment at the surface of oxides is essential for controlling both catalytic activity and long-term stability [5-8]. For instance, the high catalytic activity of $La_{0.8}Sr_{0.2}CoO_{3-\delta}$ (LSC) thin films relative to bulk polycrystalline samples is strongly coupled to the enrichment of strontium within the near-surface region of the film [4, 7, 9, 10]. However, studies on films of increased strontium content ($La_{0.6}Sr_{0.4}CoO_{3-\delta}$ and $Sr_2Co_2O_{5+\delta}$) reported no further improvements to the catalytic activity [11, 12]. Understanding the chemical nature of this strontium surface species and the physical origin of its catalytic enhancement would therefore generate new insights into developing high-performance oxide electrocatalysts.

Synchrotron facilities now provide a unique venue for investigating surface chemistry *in situ* using near-ambient pressure X-ray photoelectron spectroscopy (NAP-XPS). The combination of a high-intensity X-ray source and a differentially pumped electrostatic lens system allows studies to be performed at near-ambient pressures ($< 10^{-2}$ atm) [13] and elevated temperatures (up to 750 °C). By varying the incident photon energy to probe different information volumes, we previously identified the presence of a distinct strontium chemical environment(s) near the surface of LSC thin films (Fig. 1a) [4, 10, 14]. Other studies have observed similar behavior using *ex situ* angle-resolved depth profiling [8, 15, 16]. This "surface" strontium species increased in quantity with increasing temperature and has been suggested to play a critical role in promoting oxygen electrocatalysis on these surfaces. Strontium segregation to the surface has also been probed using acid etching and inductively coupled plasma [17], and the presence of strontium-rich perovskite particles ($SrCoO_x$) was detected at the surface of the film using anomalous X-ray scattering measurements [18]. Although many studies have suggested that there may be secondary phases such as $SrCO_3$ or $Sr(OH)_2 \cdot 8H_2O$ on the surface due to the presence of XPS peaks distinct from the LSC perovskite [8, 15], binding energies reported to date are largely similar and therefore insufficient for determining the chemical environment of the "surface" strontium (Fig. 1b) [15, 19]. It remains to be shown whether the "surface" strontium is truly a chemically distinct secondary phase or the now-known $SrCoO_x$ at the surface, the binding energy of which has not been carefully investigated to date.
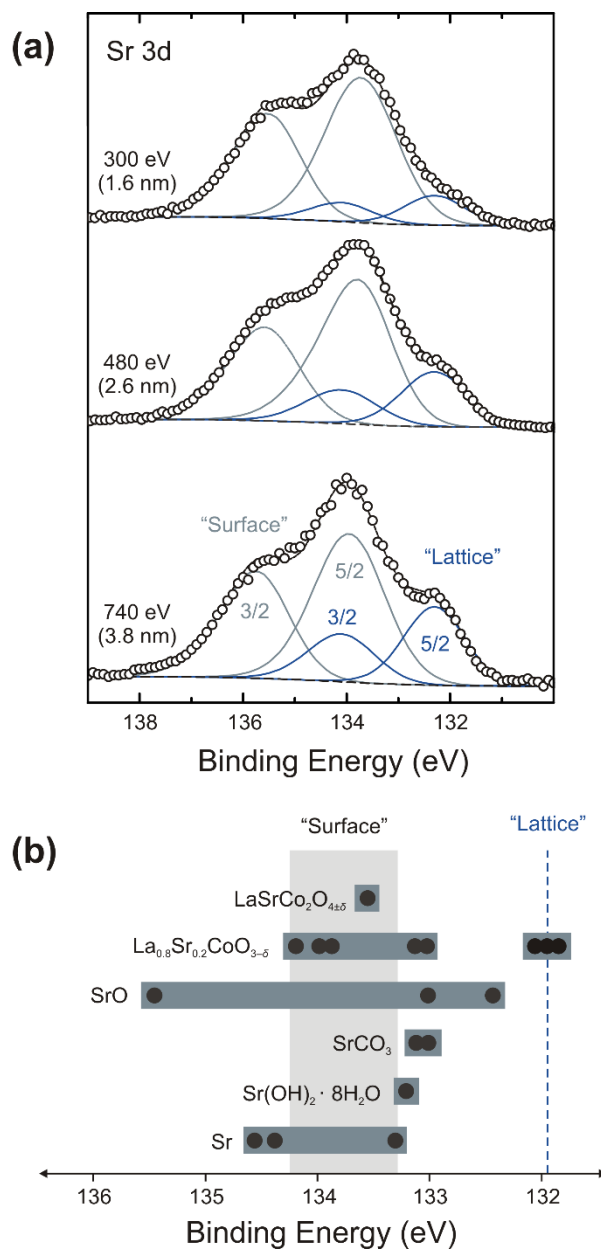
Figure 1. Summary of surface chemistry studies on $La_{0.8}Sr_{0.2}CoO_{3-\delta}$ examined for solid oxide fuel cell applications. (a) NAP-XPS Sr 3d spectra of $La_{0.8}Sr_{0.2}CoO_{3-\delta}$ film grown on yttria-stabilized zirconia at 370 °C in 760 mTorr O_2. Distinct "surface" and "lattice" components were resolved using differential energy depth-profiling. (b) Binding energies reported for various strontium chemical environments. The "surface" and "lattice" components to the Sr 3d spectra reported in (a) are also illustrated. Figures adapted from refs. [10, 20].

In this article, we perform systematic investigations of the nature of the $SrCoO_x$ surface particles using model brownmillerite $Sr_2Co_2O_5$ (SCO) epitaxial thin films grown by pulsed laser deposition (PLD) on Nb-doped $SrTiO_3$ single crystals (Nb-STO). We investigated the surface

4

chemistry of these films using NAP-XPS as a function of temperature in an oxygen environment in order to elucidate the characteristic binding energies and how these change as a function of the chemical potential of oxygen. Due to the presence of anisotropic oxygen vacancy channels in SCO, the exposure of these high-diffusion pathways to the surface can greatly impact the kinetics of oxygen incorporation and transport at the surface. As the crystallographic orientation between surface strontium-rich phases and LSC thin films is unknown, we also explore two crystallographic facets of SCO and their resultant surface chemistry, which may contribute to the enhanced activity observed for thin film surfaces.

2   Experimental

2.1 Thin film fabrication and characterization

Epitaxial thin films of 25 nm-thick SCO were fabricated by pulsed laser deposition (PLD) on single crystal (001)- and (011)-oriented 0.5 wt% Nb:SrTiO$_3$ (Nb-STO) substrates with dimensions of $10 \times 5 \times 0.5$ mm^3 (Crystec, GmbH). PLD was performed using a KrF excimer laser (λ = 248 nm) at a pulse repetition rate of 10 Hz and laser fluence of ~1.7 J cm^{-2}. The films were deposited at 750 °C under 100 mTorr O$_2$. The growth method is described in more detail elsewhere [12, 21].

Details on the structure, crystallographic orientation, and epitaxial relationship were characterized by a four-circle X-ray diffractometer (PANalytical) in on- and off-axis configurations (Fig. S1, Supplementary Information). The out-of-plane lattice constant of SCO on (001) Nb-STO was measured to be a_{pc} = 3.935 Å (where "pc" denotes the pseudocubic unit cell dimension), consistent with values reported for bulk Sr$_2$Co$_2$O$_5$ [22, 23]. SCO grows with the (001) orientation on (001) Nb-STO, with vacancy channels lying in the plane of the film (Fig. S1, Supplementary Information). Conversely, SCO grows in the (114) orientation on (011) Nb-STO, with vacancy channels oriented out of the film plane [12].

2.2 Near-ambient pressure X-ray photoelectron spectroscopy

NAP-XPS was performed at Beamline 11.0.2 at Lawrence Berkeley National Laboratory's Advanced Light Source [24]. All data were collected from a single beamtime under multibunch operation to minimize systematic errors resulting from beam flux and chamber cleanliness. SCO films (5×5 mm^2) were placed directly onto a ceramic heater and held in place by spring-loaded Iconel tips [25]. A piece of gold foil was secured on the sample surface by one of the clips to ground the sample and calibrate the binding energies. The binding energies observed are consistent with those obtained from powder measurements calibrated to the C 1s, suggesting minimal influence of sample charging [26]. A thermocouple was mounted directly onto the sample surface using the other clip for temperature measurements and isolated from the sample holder clip with an Al$_2$O$_3$ spacer.

The Sr 3d, O 1s, Co 2p, and C 1s spectra were collected under all conditions and referenced to the Au 4f binding energy (84.0 eV). The samples were cleaned by heating to 300 °C in 100

mTorr O_2 (measured by a calibrated membrane pressure gauge) until all carbon was removed, as verified by the NAP-XPS of the C 1s core level. No carbon was observed under any subsequent conditions. Differential energy measurements (accessing photoelectron kinetic energies ranging from ~200 eV to ~450 eV for both the Sr 3d and O 1s) were performed to obtain depth-resolved information on spectral contributions. Information depths, referred to in parentheses following incident photon energies, were taken as the distance necessary to collect 95% of the signal, estimated using the inelastic-mean-free path (NIST Inelastic-Mean-Free Path Database, Gries G1 equation) [27].

A series of isobaric experiments in oxygen were performed to examine the changes in surface chemistry as a function of temperature. Scans were performed at 300, 400, 500, and 600 °C in 100 mTorr O_2, remaining below the transition temperature to the hexagonal $SrCoO_3$ phase (653 °C) [28]. The sample was allowed to equilibrate for ~15 min prior to characterization. Through the use of a beam shutter, the sample was not irradiated by X-rays between scans. Care was also taken to reduce the incident photon flux so issues such as carbon deposition were not observed. Beam effects were initially observed to modify the surface oxygen species over time (Fig. S3, Supplementary Information); the data reported here in the main text was collected after adjusting the flux to mitigate beam damage.

To quantify the different surface species found on the SCO surface, O 1s spectra were deconvoluted with Gaussian−Lorentzian peaks after a Shirley-type background subtraction. The O 1s spectra were fit using three peaks; the choice of this fitting methodology can be seen directly from the raw spectra and is discussed in more detail later. The peak-fitting parameters are summarized in Table S1, Supplementary Information.

3   Results and Discussion

3.1 Temperature dependence of Sr 3d and O 1s XPS spectra for (001) SCO on (001) Nb-STO

Across the range of temperatures studied, the Sr 3d spectra for SCO looks markedly different from those of LSC films reported previously (Fig. 1a), where two distinct Sr species varied in depth-distribution with temperature. In contrast to LSC, only minor changes in the relative weighting of the features occur as a function of temperature. In particular, the distinct "lattice" component near binding energy (E_B) = 132 eV for the Sr $3d_{5/2}$ peak reported previously for LSC [10] is completely absent for SCO (Fig. 2 right). Furthermore, there is no detectable difference between the Sr 3d spectra collected at hv = 350 eV (1.8 nm) and hv = 550 eV (2.6 nm), indicating that the strontium chemical environment is homogeneous within the top 2.6 nm. Given the homogeneity of large depth probed, it is unlikely that this strontium species is a secondary phase, indicating that the Sr $3d_{5/2}$ peak of SCO is indeed chemically distinct from that of LSC. The Sr 3d and O 1s binding energies of SCO are distinct from that of the LSC lattice, and located within the range of the "surface" feature in LSC; this observation supports that particles formed on the surface of LSC during ORR relevant conditions are SCO-like. Nevertheless, it should be noted that the binding energy alone cannot be used to distinguish strontium in the SCO particles

on the surface of LSC from other potential secondary phase contributions (*e.g.*, strontium hydroxides) due to their similar core level shifts.

At 300 °C, the O 1*s* spectrum shows two primary features at E_B ~529.9 and ~531.9 eV (Fig. 2 left). The peak at E_B ~529.9 eV can be assigned to the bulk oxide peak (hereafter referred to as "lattice"), which is ~1 eV higher than values of related perovskite chemistries reported previously [10, 29]. The peak at higher binding energy can be assigned to a surface species (denoted as "surface"), as evident from the reduction in intensity for spectra collected at $hv = 735$ eV (2.1 nm) relative to those collected at $hv = 1000$ eV (3.6 nm). We have observed a similar feature in the O 1*s* of $LaCoO_3$ thin films, where this binding energy shift for oxygen surface species relative to bulk perovskite oxide ions can be attributed to either shifts in the Madelung potential at the surface and/or surface electronic/structural reconstruction [29].
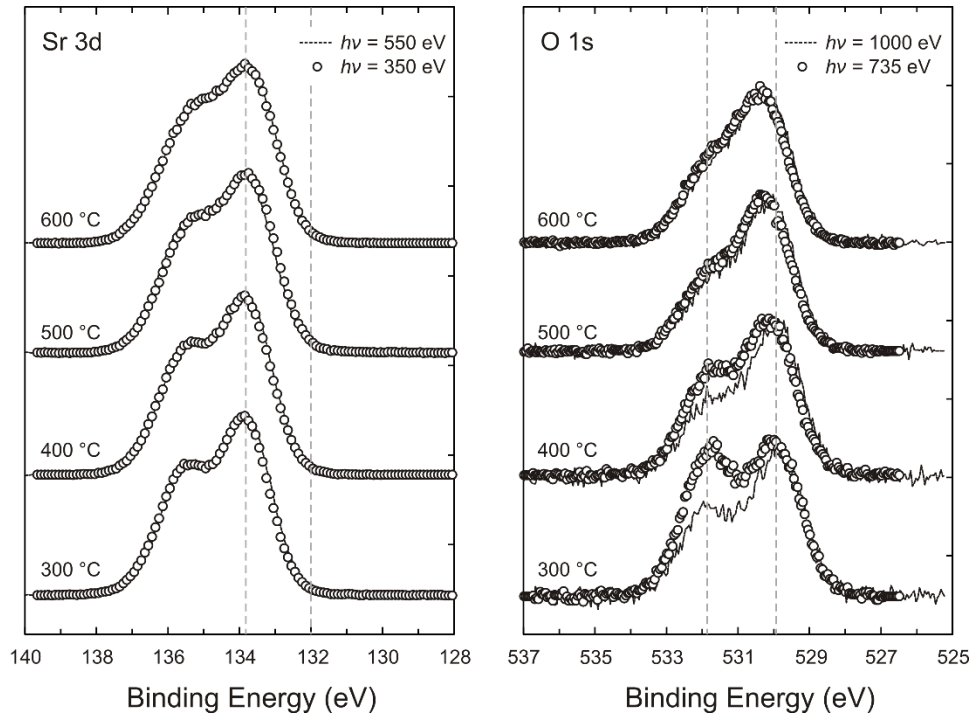

Figure 2. Temperature dependence of (001) SCO grown on (001) Nb-STO in 100 mTorr oxygen, contrasting shallow (black circle) and deeper (black dashed line) information depths reached by the noted incident photon energies. Gray dashed lines illustrate the positions of noted features. (left) Sr 3d spectra show a uniform chemical environment for the top 2.6 nm (line) and top 1.8 nm (circles). The doublet at ~133.9, ~135.9 eV corresponds to the Sr $3d_{5/2}$, $3d_{3/2}$ spin-orbit splitting, and no Sr $3d_{5/2}$ feature is apparent at ~132 eV where the LSC "lattice" component is expected. (right) O 1s spectra show a "lattice" species at ~529.9 eV and a "surface" species at ~531.9 eV, where the intensity of the "surface" species increases as the probing depth decreases from 2.9 nm (line) to 1.7 nm (circles) and decreases with temperature. All measurements were collected at the same spot with acquisition times of less than 2 minutes per spectra.

Substantial changes in the O 1s spectra of the SCO surface were observed with increasing temperature. The "surface" peak of O 1s decreased substantially with increasing temperature from 300 to 500 °C, and at temperatures greater than 500 °C, the relative contribution of the surface peak to the bulk oxide peak does not change significantly with incident X-ray energy, indicating that species within the film are homogeneously distributed within the ~3 nm information depth. Thus, while the contribution at E_B ~529.9 eV is preferentially located at the surface at 300 °C, it is either located homogenously throughout the sample at higher temperatures, or its binding energy is coincident with another distinct species which convolutes the depth profile. The former case of surface enrichment at low temperatures and homogeneous distribution at high temperatures would be consistent with, for instance, the filling of oxygen vacancies at the surface in a thermally activated process.

3.2 Temperature dependence of Sr 3d and O 1s XPS spectra for (114) SCO on (011) Nb-STO

Films grown on (011) Nb-STO have vacancy channels oriented out of the plane of the film [12]. This leads to some marked differences in the surface chemistry in contrast to films grown on (001) Nb-STO (Fig. 3). In the Sr 3d spectra, the features begin to broaden as temperature increases, and a distinct feature at lower binding energy becomes apparent at 600 °C. The binding energy of this feature is consistent with the "lattice" component reported previously for LSC thin films, and does not correspond to any of the Sr-rich secondary phases in Fig. 1.

At temperatures lower than 400 °C, the O 1s spectra of (001) and (114) SCO surfaces look similar. However, as the Sr 3d spectra of the (114) SCO film broaden with increased temperature, the O 1s spectra also broaden at the low binding energy side, with a distinct shoulder located at ~528.6 eV becoming apparent at 600 °C. The binding energy of this feature is similar to that of the LSC "lattice" oxygen [10, 15], and its relative intensity does not change with information depth. Together, the new features of the Sr 3d and O 1s from (114) SCO film coincident with that of the perovskite LSC lattice suggest that the brownmillerite surface can incorporate oxygen at high temperatures, and that the exposed oxygen vacancy channels enable fast diffusion into the bulk with "surface" oxygen species remaining present on the surface at high temperatures [12]. Note that the "surface" oxygen feature decreases in relative intensity as the temperature increases until 500 °C, then increases again at 600 °C. We discuss this behavior and compare it with that of the (001) SCO film in detail later.
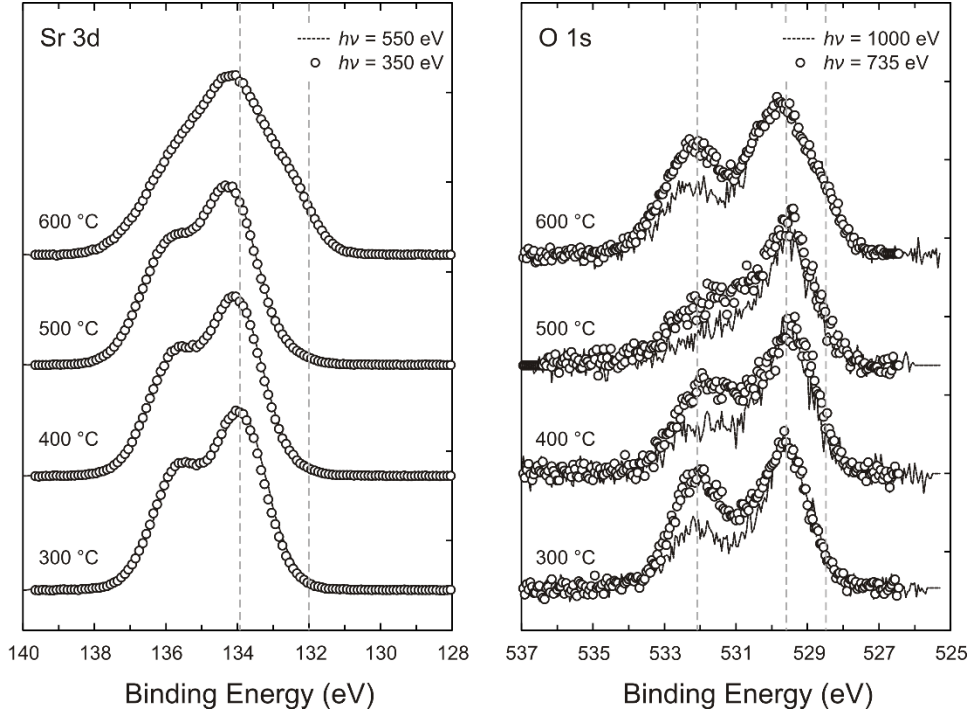
Figure 3. Temperature dependence of (114) SCO grown on (011) Nb-STO in 100 mTorr oxygen, contrasting shallow (black circle) and deeper (black dashed line) information depths reached by the noted incident photon energies. Dashed gray lines illustrate the positions of noted features. (left) Sr 3d spectra show a uniform chemical environment for the top 2.4 nm (line) and top 1.5 nm (circles); a Sr 3d$_{5/2}$ feature at ~133.9 eV is present under all conditions and an additional feature appears at 600 °C coinciding with the LSC "lattice" at ~132 eV. (right) O 1s spectra show a "lattice" species at ~529.9 eV and a "surface" species at ~531.9 eV, where the intensity of the "surface" species increases as the information depth decreases from 3.6 nm (dashed) to 2.1 nm (circles). A new feature appears at 600 °C, located at ~528.6 eV, close to that of the LSC "lattice." All measurements were collected at the same spot with acquisition times of less than 2 minutes per spectra.

3.3 Influence of temperature on the electronic structure

While the Sr 3d and O 1s for SCO grown on both (001) and (011) Nb-STO are largely similar at low temperatures, some differences exist in the Co 2p satellite features. These Co 2p spectra were fitted using the cluster model methodology of Bocquet *et al.* [30], which can elucidate differences in the electronic structure, parametrized by the onsite *d-d* Coulomb repulsion energy (*U*), charge transfer energy (Δ), and ligand *p* − Co *d* transfer integral (*pdσ*). Fig. 4 shows the background subtracted data and simulations performed assuming an average oxidation state of 3+, fitting these parameters and incorporating core-hole interactions and broadening to simulate the spectra. Comparing the satellite intensities at 300 °C, a greater intensity ~5 eV from the main peak for (001) SCO is observed versus the lower intensity centered ~7 eV from the main peak for (114) SCO. Furthermore, examining the temperature-dependent differences in the raw Co 2p

spectra, the satellite feature for the (001) SCO becomes more pronounced as temperature increases – most evident when comparing the 300 °C and 600°C spectra. In contrast, very little change is observed in the (114) SCO spectra. These differences are observable in the simulated spectra as well. The origin to these features can be discerned through the fitting parameters of the simulations, where the dominant satellite feature reflects a predominantly $|\underline{c}\ t_{2g}^{5}e_{g}^{1}\rangle$ character in the final state, in contrast to the primarily $|\underline{c}\ t_{2g}^{5}e_{g}^{2}\ \underline{L}\rangle$ character of the main peak (where $\underline{c}$ represents the Co 2p core hole and $\underline{L}$ represents a ligand hole).
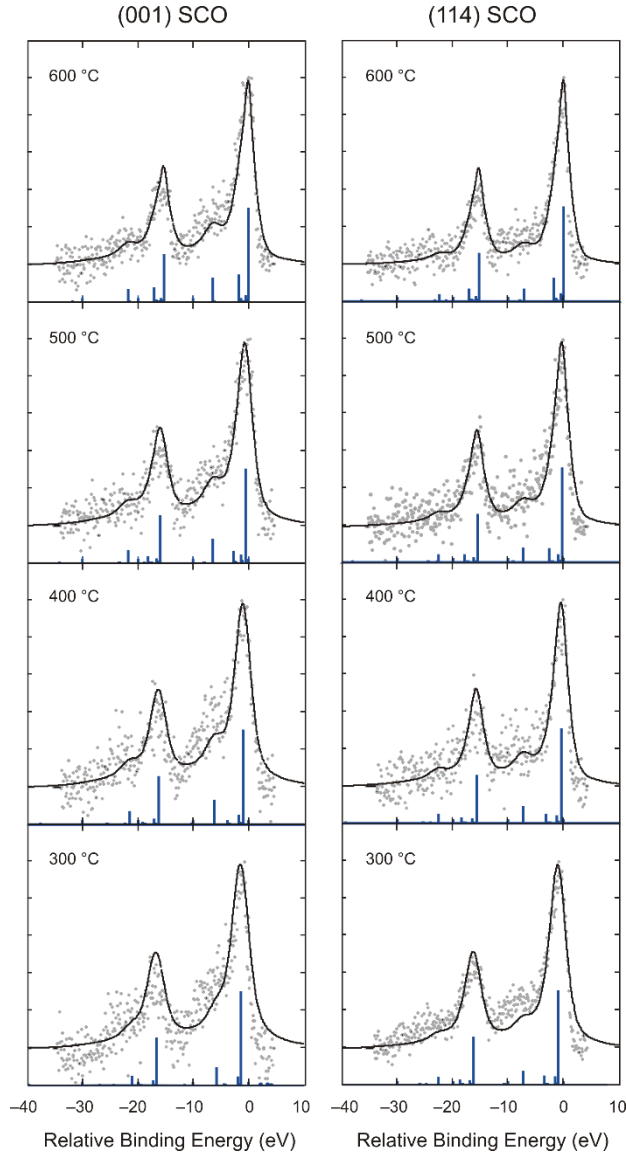

Figure 4. Co 2p spectra in 100 mTorr oxygen for SCO from NAP-XPS at 1000 eV (1.8 nm, light gray circles) and simulations (black lines) for (left) (001) SCO grown on (001) Nb-STO and (right) (114) SCO grown on (011) Nb-STO. Excitations and relative energies are shown below (blue bars). Cluster model fittings following the method of Bocquet *et al.* [30] assumed an average oxidation state of 3+ and were parametrized by the onsite *d-d* Coulomb repulsion energy

10

(U), charge transfer energy (Δ), and Slater-Koster parameter ($pd\sigma$), reflecting the hybridization of the O 2p orbitals with the metal d orbitals. Simulated spectra use a Lorentzian broadening of 1.5 eV, Gaussian broadening of 1.4 eV, and core-hole interaction $Q = U/0.83$ as implemented by Bocquet *et al* [30]. All measurements were collected at the same spot with acquisition times of ~10 minutes per spectra.

The cobalt electronic structure information obtained from cluster-model fittings provides important insights into these changes and the energetics for oxygen incorporation. Fig. 5 shows changes in U, Δ, and ($pd\sigma$) as a function of temperature. The (114) SCO grown on (011) Nb-STO (Fig. 5a) has considerably higher U but comparable Δ (Fig. 5b) and ($pd\sigma$) (Fig. 5c) in contrast to (001) SCO grown on (001) Nb-STO. As U describes the onsite d-d Coulomb repulsion energy of the transition metal, this suggests that Co plays an integral role in distinguishing the behavior of the two SCO orientations given their comparable Co-O overlap and charge transfer energy. While no significant changes were observed in U or ($pd\sigma$) as a function of temperature, notable differences were observed in temperature dependence of Δ for the two surfaces. As the temperature increases, Δ increases for both the (001) and (114) SCO. This finding is consistent with the aforementioned changes observed in the satellite features of the raw spectra. Changes in Δ likely reflect the influence of oxygen non-stoichiometry on the metal-ligand charge transfer (as δ decreases, the oxidation state decreases and Δ increases [31, 32]). Increases in Δ as a function of temperature therefore indicate increases in oxygen non-stoichiometry. Such changes in the electronic structure weaken the ability of lattice oxygen ions to reduce the transition metal ions and makes it more difficult to form oxygen ligand holes [31]. Both effects are known to increase the energy of oxygen vacancy formation [33, 34], which can directly modify the activation energy for the ORR [35, 36].
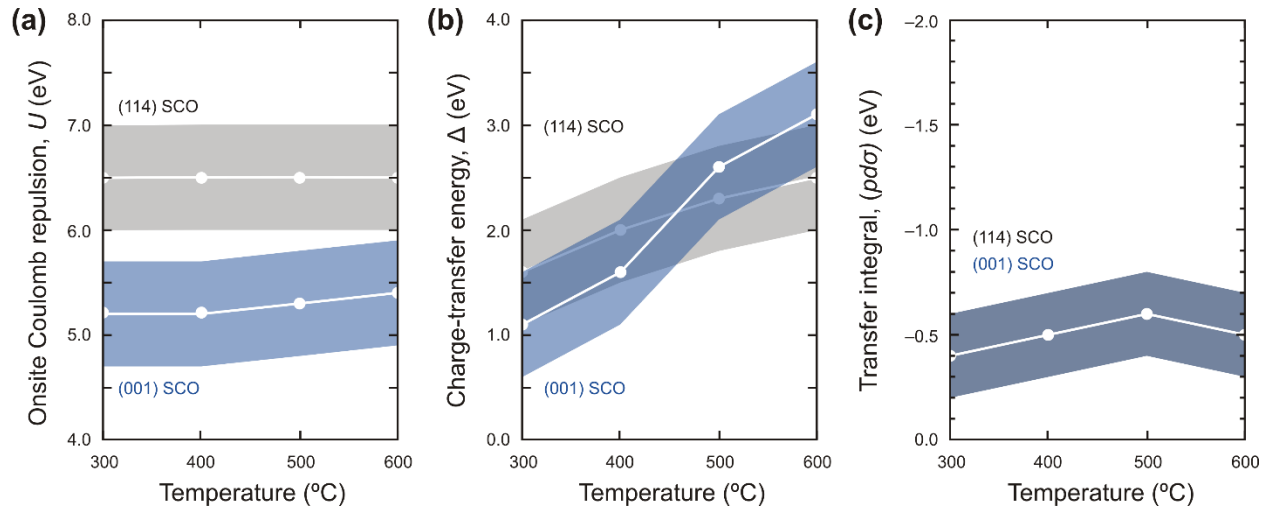

Figure 5. Temperature-dependent differences in cobalt electronic structure from cluster-model fittings in Fig. 4. White lines illustrate the fitted values as a function of temperature with shaded regions representing the estimated error. Error estimates of the simulations use values given by

Bocquet *et al.* [30]. (001) SCO is shown in black and (114) SCO is in gray. (a) The *d-d* Coulomb repulsion (*U*) remains roughly constant with temperature for both surfaces; (b) the charge-transfer energy (Δ) increases with temperature, suggesting a change in oxygen non-stoichiometry; and (c) the ligand−metal transfer integral (*pdσ*) remains roughly constant and comparable for both surfaces.

3.4 Implications for oxygen electrocatalysis

We now bring back this new understanding of the electronic structure of SCO films to oxygen electrocatalysis. Previous measurements have shown orienting the oxygen vacancy channels out of plane on (114) SCO leads to a reduced area specific resistance and enhanced surface oxygen exchange rate (k_{chem}) for oxygen reduction at high temperatures relative to in plane channel orientation on (001) SCO [12]. Deconvolution of the O 1*s* spectra can be used to determine the relative quantities of surface oxygen species and oxygen in the bulk of the SCO film (Fig. 6; details provided in Fig. S5). The relative quantity of surface oxygen species reaches a minimum near 500 °C for both film orientations, increasing again at 600 °C. In addition, at high temperatures of 600 °C, the (114) SCO develops a new feature at lower binding energies close to that of the LSC lattice while the (001) SCO shows little change in the main oxide peak. This suggests that the (114) SCO has a lower activation energy for oxygen vacancy formation and oxygen incorporation, promoting filling of vacancies located at tetrahedral cobalt sites at elevated temperatures. The activation temperature for this process (between 500 °C and 600 °C) is corroborated by previous measurements by Vashook *et al.* [37] of the oxygen sorption/desorption temperature in SCO ceramics (~500 °C). These experiments provide the first detailed account of the chemical nature of oxygen species that are desorbed at elevated temperatures. The facile kinetics of oxygen exchange on SCO may therefore contribute to the enhanced activity observed on LSC films with Sr enrichment at the surface.
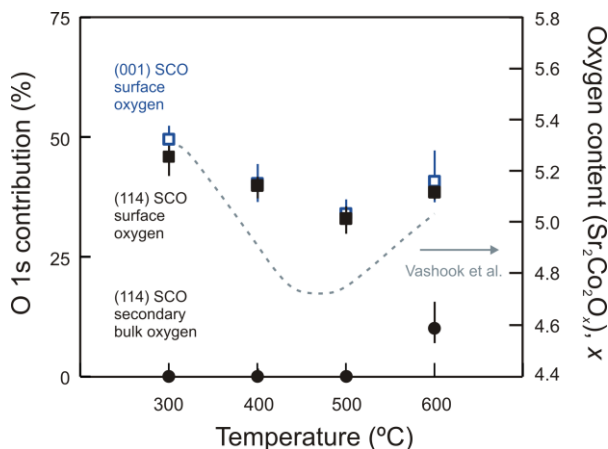

Figure 6. Oxygen species present on (001) SCO (open blue) and (114) SCO (filled black) as a function of temperature. The quantity of surface oxygen species (square) reaches a minimum at 500 °C, increasing again (black circles). This trend parallels the oxygen content, shown as

dashed, measured by Vashook *et al.* [37]. At 600 °C a secondary bulk oxygen feature (black circles) becomes prominent in the (114) SCO. Error bars are defined as the 95% confidence intervals as estimated from Monte Carlo simulations of the experimental noise. Details on the error analysis employed have been discussed elsewhere [29].

We also observed a large change in Δ of the SCO films as a function of temperature, indicating a change in oxygen non-stoichiometry consistent with increasing activation energy for oxygen incorporation. This suggests that stabilizing higher oxygen contents in the SCO structure through the substitution of cobalt (e.g. with iron) may promote higher activities, which may explain the high activities of cobalt-ferrites such as $La_{0.6}Sr_{0.4}Co_{0.6}Fe_{0.4}O_{3-\delta}$ [38] and $Ba_{0.5}Sr_{0.5}Co_{0.8}Fe_{0.2}O_{3-\delta}$ [39].

4   Conclusion

In summary, we demonstrated key differences in the surface chemistry for SCO films of different orientations by using NAP-XPS, which can be a powerful tool for studying model systems and gaining additional insights into catalytic processes. We found that the Sr 3d and O 1s binding energies are consistent with those of surface species reported in previous LSC systems; consequently, it is difficult to say from XPS alone whether previous NAP-XPS studies on LSC observed the formation of secondary phases or simply the segregation of an SCO phase. Detailed analysis of the Co 2p spectra suggests that the SCO films lose oxygen as a function of temperature. Moreover, deconvolution of the O 1s spectra shows distinct behavior for (114) SCO compared to (001) SCO, where an additional bulk oxygen species is observed. These findings indicate a change to a perovskite-like oxygen chemistry that occurs more easily in (114) SCO than (001) SCO, likely due to the orientation of oxygen vacancy channels out-of-plane with respect to the film surface. This difference in surface chemistry is responsible for the anisotropy of the oxygen surface exchange coefficient of SCO and may contribute to the enhanced ORR kinetics of LSC thin films observed previously.

References

1. SB Adler (2004) Chem Rev 104:4791-4843.
2. WC Chueh, SM Haile (2012) Annu Rev Chem Biomol Eng 3:313-341.
3. EJ Crumlin, E Mutoro, SJ Ahn, J la O' G, DN Leonard, A Borisevich, MD Biegalski, HM Christen, Y Shao-Horn (2010) J Phys Chem Lett 1:3149-3155.
4. E Mutoro, EJ Crumlin, MD Biegalski, HM Christen, Y Shao-Horn (2011) Energy Environ Sci 4:3689.
5. W Lee, JW Han, Y Chen, Z Cai, B Yildiz (2013) J Am Chem Soc 135:7909-7925.
6. H Ding, AV Virkar, M Liu, F Liu (2013) Phys Chem Chem Phys 15:489-496.
7. J Druce, H Tellez, M Burriel, MD Sharp, LJ Fawcett, SN Cook, DS McPhail, T Ishihara, HH Brongersma, JA Kilner (2014) Energy Environ Sci 7:3593-3599.
8. Z Cai, M Kubicek, J Fleig, B Yildiz (2012) Chem Mater 24:1116-1127.
9. J la O' G, SJ Ahn, E Crumlin, Y Orikasa, MD Biegalski, HM Christen, Y Shao-Horn (2010) Angew Chem Int Ed Engl 49:5344-5347.
10. EJ Crumlin, E Mutoro, Z Liu, ME Grass, MD Biegalski, Y-L Lee, D Morgan, HM Christen, H Bluhm, Y Shao-Horn (2012) Energy Environ Sci 5:6081.
11. EJ Crumlin, SJ Ahn, D Lee, E Mutoro, MD Biegalski, HM Christen, Y Shao-Horn (2012) J Electrochem Soc 159:F219-F225.
12. H Jeen, Z Bi, WS Choi, MF Chisholm, CA Bridges, MP Paranthaman, HN Lee (2013) Adv Mater 25:6459-6463.
13. DF Ogletree, H Bluhm, G Lebedev, CS Fadley, Z Hussain, M Salmeron (2002) Rev Sci Instrum 73:3872.
14. EJ Crumlin, E Mutoro, WT Hong, MD Biegalski, HM Christen, Z Liu, H Bluhm, Y Shao-Horn (2013) J Phys Chem C 117:16087-16094.
15. PAW van der Heide (2002) Surf Interface Anal 33:414-425.
16. H Dulli, PA Dowben, S-H Liou, EW Plummer (2000) Phys Rev B 62:14629-14632.
17. M Kubicek, A Limbeck, T Frömling, H Hutter, J Fleig (2011) J Electrochem Soc 158:B727.
18. Z Feng, Y Yacoby, WT Hong, H Zhou, MD Biegalski, HM Christen, Y Shao-Horn (2014) Energy Environ Sci 7:1166.
19. CD Wagner, AV Naumkin, A Kraut-Vass, JW Allison, CJ Powell, JR Rumble Jr, 2003.
20. E Mutoro, EJ Crumlin, H Pöpke, B Luerssen, M Amati, MK Abyaneh, MD Biegalski, HM Christen, L Gregoratti, J Janek, Y Shao-Horn (2012) J Phys Chem Lett 3:40-44.
21. H Jeen, WS Choi, MD Biegalski, CM Folkman, I-C Tung, DD Fong, JW Freeland, D Shin, H Ohta, MF Chisholm, HN Lee (2013) Nat Mater 12:1057-1063.
22. A Nemudry, P Rudolf, R Schollhorn (1996) Chem Mater 8:2232-2238.
23. A Muñoz, C de la Calle, JA Alonso, PM Botta, V Pardo, D Baldomir, J Rivas (2008) Phys Rev B 78.
24. D Frank Ogletree, H Bluhm, ED Hebenstreit, M Salmeron (2009) Nuclear Instruments and Methods in Physics Research Section A: Accelerators, Spectrometers, Detectors and Associated Equipment 601:151-160.
25. JA Whaley, AH McDaniel, F El Gabaly, RL Farrow, ME Grass, Z Hussain, Z Liu, MA Linne, H Bluhm, KF McCarty (2010) Rev Sci Instrum 81:086104.
26. P Wang, L Yao, M Wang, W Wu (2000) J Alloys Compd 311:53-56.
27. WH Gries (1996) Surf Interface Anal 24:38-50.
28. C de la Calle, A Aguadero, JA Alonso, MT Fernández-Díaz (2008) Solid State Sci 10:1924-1935.

29. KA Stoerzinger, WT Hong, EJ Crumlin, H Bluhm, MD Biegalski, Y Shao-Horn (2014) J Phys Chem C 118:19733-19741.
30. AE Bocquet, T Mizokawa, T Saitoh, H Namatame, A Fujimori (1992) Phys Rev B 46:3771-3784.
31. J Zaanen, GA Sawatzky (1990) J Solid State Chem 88:8-27.
32. JB Torrance, P Lacorre (1991) Physica C (Amsterdam) 182:351-364.
33. M Pavone, AM Ritzmann, EA Carter (2011) Energy Environ Sci 4:4933.
34. DN Mueller, ML Machala, H Bluhm, WC Chueh (2015) Nat Commun 6:6097.
35. S Adler, X Chen, J Wilson (2007) J Catal 245:91-109.
36. Y-L Lee, J Kleis, J Rossmeisl, Y Shao-Horn, D Morgan (2011) Energy Environ Sci 4:3966.
37. VV Vashook, MV Zinkevich, H Ullmann, J Paulsen, N Trofimenko, K Teske (1997) Solid State Ionics 99:23-32.
38. JE ten Elshof, MHR Lankhorst, HJM Bouwmeester (1997) Solid State Ionics 99:15-22.
39. L Wang, R Merkle, J Maier, T Acartürk, U Starke (2009) Appl Phys Lett 94:071908.